

This is the accepted manuscript made available via CHORUS. The article has been published as:

Direct Observation of Nonlinear Coupling between Pedestal Modes Leading to the Onset of Edge Localized Modes

A. Diallo, J. Dominski, K. Barada, M. Knolker, G. J. Kramer, and G. McKee

Phys. Rev. Lett. **121**, 235001 — Published 3 December 2018

DOI: [10.1103/PhysRevLett.121.235001](https://doi.org/10.1103/PhysRevLett.121.235001)

Direct Observation of Nonlinear Coupling between Pedestal Modes Leading to the Onset of Edge Localized Modes

A. Diallo,¹ J. Dominski,¹ K. Barada,² M. Knolker,¹ G.J. Kramer,¹ and G. McKee³

¹*Princeton Plasma Physics Laboratory, Princeton, NJ, USA*

²*Department of Physics, University of California, Los Angeles CA, USA*

³*Department of Engineering Physics, University of Wisconsin, Madison, WI, USA*

(Dated: October 8, 2018)

Prior to eruptive events such as edge localized modes (ELMs), quasi-coherent fluctuations, referred to as pedestal modes, are observed in the edge of fusion devices. We report on the investigations of nonlinear coupling between these modes during quasi-stationary inter-ELM phases leading to the ELM onset. Three dominant modes, with density and magnetic signatures, are identified as the key players in the triggering mechanism of certain class of ELMs. We demonstrate that one of these mode is generated by the two others through three waves interactions. The generated mode is radially shifted relative to the other two modes towards the last-closed flux surface as the ELM event approaches. Our results suggest that nonlinear coupling of pedestal modes, associated with radial distortions pushing out of the pedestal, is a possible mechanism for the triggering low frequency ELMs relevant for future fusion devices..

In nature, sporadic events leading to explosive releases of energy occur through solar flares and magnetic substorms [1]. Analogous events occur in magnetically confined fusion devices and manifest themselves as edge-localized modes (ELMs). Solar flares, magnetic substorms, and ELMs are similar as they all are quasi-stationary prior to reaching the point of explosive loss of confined plasma.

During an ELM event, the edge plasma suddenly releases a fraction of the system's stored energy over a few microseconds. ELMs are repetitive eruptions that deposit energy and particles onto the plasma facing components of tokamaks. The ELM phenomenology has been described in many reviews [2–5]. The working hypothesis for the ELM onset is the linear destabilization of ideal magnetohydrodynamic (MHD) peeling-ballooning (PB) instabilities [2, 3, 5, 6] localized in the pedestal. The pedestal is the narrow boundary layer exhibiting steep density and temperature gradients in high confinement plasma regimes.

The PB model posits that ELMs are triggered when increasing pedestal gradients reach a critical threshold. The PB model, however, cannot explain why certain ELMs are not triggered when the pedestal gradients reach the critical PB gradients and remain in a metastable state long before the ELM onset. This class of unexplained ELMs has been observed in many experimental devices [7–12] for which the onset mechanism has been largely unexplored. A nonlinear model was proposed in Refs. [13–15], where ELMs are the result of a basic detonation scenario in which a ballooning instability nonlinearly grows explosively.

This letter focuses such unexplained ELMs (hereinafter ELMs). We observe that two modes (located inside the pedestal) nonlinearly couple to a third mode near the last-closed flux surface. We identify this three-wave interaction mechanism, leading to a spatial distortion of the pedestal. The nonlinear mechanism brings the pedestal in an unstable state which triggers the ELM. The results

presented here can, in principle, be applied to many physical systems that encounter long periods of quiescence in a metastable state before an explosive event (e.g., solar prominence and magnetic substorms).

The physical mechanism leading to the onset of an ELM event is studied on the DIII-D tokamak. The discharge is a lower-single null plasma, with plasma current of 1 MA, $\beta_n \sim 1.4$, a stored energy of 0.43 MJ, and line-averaged density of $5 \times 10^{19} \text{ m}^{-3}$. In this discharge, there are two types of ELMs, high (60 Hz) and low (~ 20 Hz) frequency ELMs. The high frequency ELMs (short inter-ELM periods) are consistent with the PB model, because the ELM onset occurs when the increasing pedestal gradients reach the critical PB gradient. The low frequency ELM (long inter-ELM periods) are not consistent with the PB model because the pedestal gradients saturate near the critical PB gradient without triggering an ELM. The remainder of this letter is focused on these type I ELMy discharges with low ELM frequencies ~ 20 Hz. During these ELMs, the pedestal parameters are clamped as was observed in Refs. [7–9, 11, 16, 17]. Peeling-Ballooning calculations computed using these clamped gradients indicate that the edge pressure gradient and current are near the stability point akin to a metastable state prior to an ELM onset (see similar observations in refs. AUG [9, 10], C-Mod [8], DIII-D [11], and JET [7], and discussions by Kirk *et al.* in [12]).

The main diagnostics used in this analysis are the fast magnetic probes measuring fluctuations in the poloidal magnetic field (referred to as \hat{B}_θ) and the spatially resolved beam-emission spectroscopy (BES) diagnostic probing the local density fluctuations [18] (referred to as δn_e). Figure 1(a) displays the magnetic spectrograms showing quasi-coherent fluctuations between ELMs. This figure shows multiple modes between ELMs. Fig. 1(b) represents a zoomed in version of the denoised spectrogram identifying the three dominant modes. Each mode's amplitude and frequency are tracked between ELMs. Core modes, whose amplitudes are not affected by the

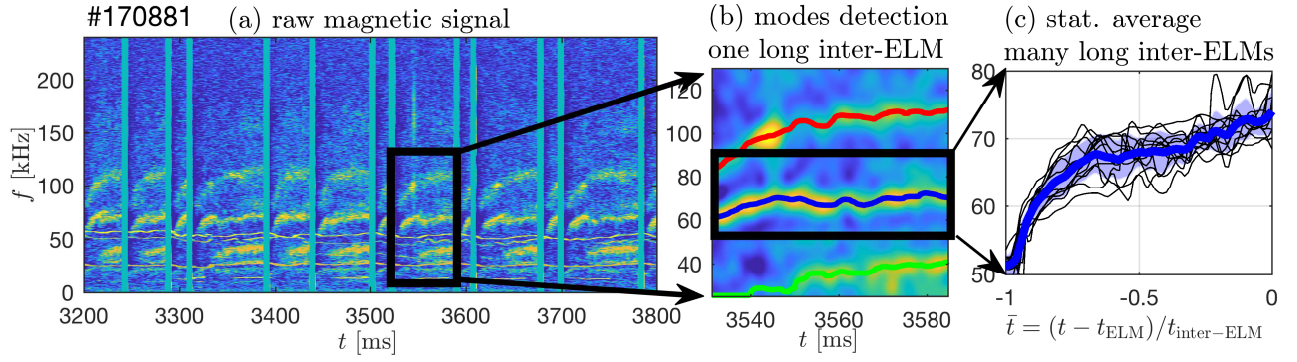


FIG. 1. Example spectrogram of the magnetic fluctuations for shot 170881. (a) Magnetic spectrogram during multiple ELMs. Here the ELMs are represented by the thick vertical lines. Typical rise time of these ELMs is $\simeq 80\mu s$. (b) Zoomed spectrogram over a shorter time window where the core modes have been filtered out. (c) Example of statistical average (blue) on multiple long inter-ELM periods (black). The horizontal axis represents the time relative to the ELM onset \bar{t} .

ELMs, are excluded from the analysis.

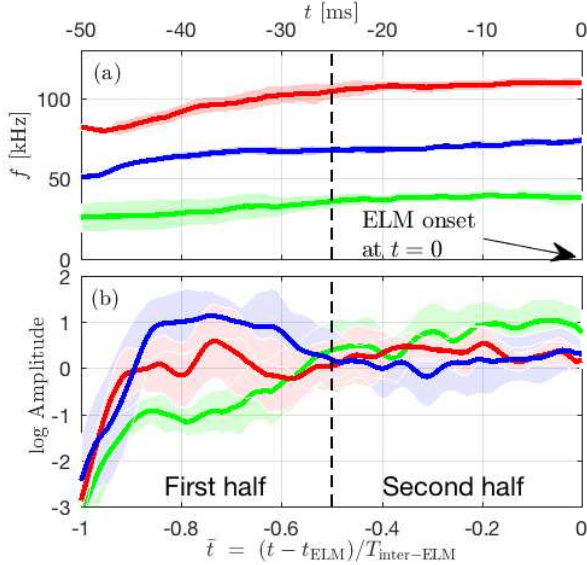


FIG. 2. Dynamics of the frequency and amplitude of the three dominant modes observed in magnetic fluctuations as a function of ELM cycle [the time relative to an ELM in ms is on the top horizontal axis for reference]. The reference $t = 0$ is located at the ELM onset. (b) Associated mode amplitude evolution during the ELM cycle, in log-scale. These quantities have been statistically averaged over multiple inter-ELM periods. The shaded area represents the standard deviations. The same color code for the three modes is used throughout the paper.

The inter-ELM dynamics of the most dominant modes are studied in detail using the signals from $\partial_t \tilde{B}_\theta$ with high signal to noise ratio (SNR). We systematically track their amplitude and frequency following local maxima of the spectrogram up to the ELM event, and we compute the statistical average of the dominant mode amplitude and frequency over multiple long inter-ELMs. Fig. 1(c) shows the various inter-ELM time traces of the blue mode frequency and their averages as a function of the normalized

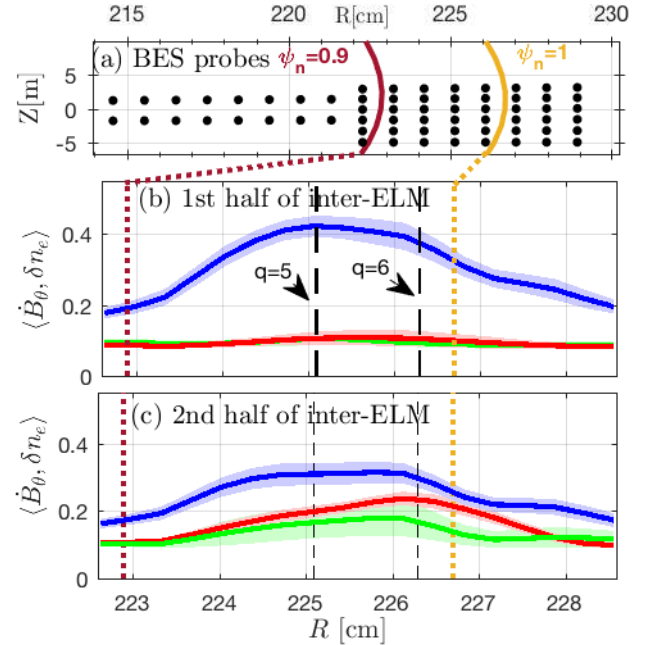


FIG. 3. Radial profiles during the ELM cycle. (a) 2D map of the BES locations for reference spanning the edge plasma (including the pedestal $\psi_n = 0.9 - 1.$). (b) Frequency resolved radial profiles of the three dominant modes using correlation between magnetic probe (\dot{B}_θ) and BES probes (δn_e) during the first half of the ELM cycle and (c) during the last phase of the ELM cycle.

ELM period: $\bar{t} = (t - t_{\text{ELM}}) / t_{\text{inter-ELM}}$ and $t_{\text{inter-ELM}}$ is the duration of each inter-ELM period [$\bar{t} = 0$ corresponds to the ELM onset.] Here, figure 2(a) displays these mode frequencies and Fig. 2(b) shows the associated amplitude evolution leading up to ELMs.

The timeline leading to the ELM onset can be summarized as function of the ELM cycle. During the first half ($\bar{t} < -0.5$): the mode at $\simeq 69$ kHz (blue) onset is correlated with the temperature pedestal gradient recovery (such correlation was shown in Refs. [9, 11]) and grows

until its amplitude saturates. Similarly, the $\simeq 100$ kHz (red) mode amplitude fluctuates with a peak at $\bar{t} = -0.7$; and the ~ 39 kHz (green) mode starts growing from $\bar{t} \simeq -0.8$. *During the second half:* the blue mode, which started to decay near $\bar{t} = -0.6$, saturates near $\bar{t} = -0.3$; the red mode amplitude increases by near an order of magnitude until saturation, and the ~ 39 kHz (green) mode continues to increase until saturation at the very end of the ELM cycle $\bar{t} \gtrsim -0.9$.

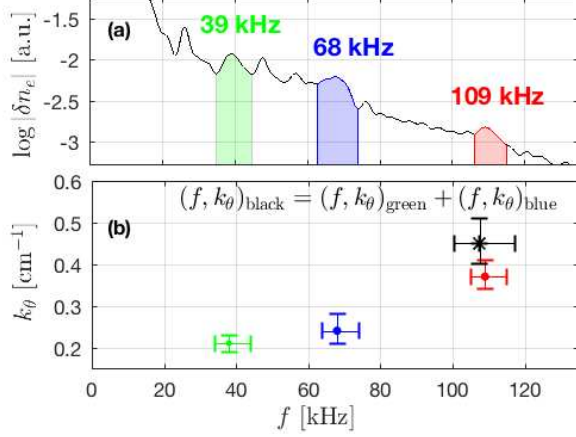


FIG. 4. (a) BES time-averaged power spectra over the last phase of the ELM cycle. The three dominant modes, colorblue observed in the magnetic spectrogram - Fig. 1, are indicated with the color codes. (b) The measured poloidal wave vector k_θ of the three identified modes - color code: green for the mode $f \simeq 39$ kHz, blue for the mode $f \simeq 68$ kHz, and red for the mode $f \simeq 109$ kHz. The black asterisk is positioned at $(f, k_\theta)_{\text{black}}$ such that $f = f_{\text{Green}} + f_{\text{Blue}}$ and $k_\theta = k_{\theta, \text{Green}} + k_{\theta, \text{Blue}}$ (see Fig. 5 and associated discussions in text).

To further characterize the radial profiles of these three modes and their evolution during the first and second half of the ELM cycles, we analyze the correlation between the magnetic fluctuations \dot{B}_θ and the density fluctuations δn_e [measured using the BES system at the positions illustrated in Fig. 3(a)].

Figures 3 (b) and (c) display the radial profiles of the modes during the first and second half of the ELM cycle, respectively. The three dominant modes' contributions to $\langle \dot{B}_\theta, \delta n_e \rangle$ indicate a transition from a dominant contribution of the blue mode during the first half of the ELM cycle (see Fig. 3(b)) towards a more balanced contribution between the three modes during the second half (see Fig. 3(c)). From the first half to the second one, the blue mode shows a loss in correlation $\langle \dot{B}_\theta, \delta n_e \rangle$ while the green and red modes display an increase of correlation.

The red mode that peaks near the $q = 6$ surface (see Fig. 3(c)), in contrast to the blue and green modes which peak near $q = 5$ flux surface. Given that this correlation provides a proxy for the location of the modes, Fig. 3(c) shows an **outwards shift of the red mode toward the last-closed flux surface**. We now investigate the underlying mechanism leading to growth of the red mode.

Energy transfer through three-wave interaction between the dominant modes can explain the growth of the red mode following the relation:

$$(f, k_\theta)_{\text{green}} + (f, k_\theta)_{\text{blue}} \simeq (f, k_\theta)_{\text{red}}. \quad (1)$$

In the above equation, the frequencies and wavenumbers are measured using BES (see caption of Fig. 4 for more details). The left-hand side of Eq. (1) is represented by the black asterisk in Fig. 4(b) which agrees within errorbar with $\simeq (f, k_\theta)_{\text{red}}$. This analysis suggests that the green and blue modes are coupled to provide energy to the red mode.

The three-wave interaction can be described using the Ritz model [19] (sec. IV), where the evolution of a mode's amplitude is given by:

$$\frac{\partial P_f}{\partial t} \simeq 2\gamma_f P_f + \sum_{f_1, f_2} T_f(f_1, f_2), \quad (2)$$

where f is the frequency of the mode, γ_f its linear growth rate, P_f its power, and f_1 and f_2 are the frequencies of the other modes composing the triad $f = f_1 + f_2$ leading to the transfer of energy $T_f(f_1, f_2)$. Such nonlinear coupling can *either* lead to the merge of two waves of frequencies f_1 and f_2 into a wave of frequency f ; or it can result in the decay of the wave of frequency f into two waves of frequencies f_1 and f_2 .

One useful tool, enabling analyses of the nonlinear coupling between modes and the energy transfer T_f , is the bicoherence b^2 applied to the magnetic signal \dot{B}_θ (for simplicity we let $\dot{B}_\theta = S$). **The bicoherence is a standard analysis technique that has been applied in turbulence studies of laboratory magnetized plasmas [20–24]**, and is defined as (see Ref. [25]):

$$b^2 = \frac{|\langle S_{f_1} S_{f_2} S_{f_1+f_2}^* \rangle|^2}{\langle |S_{f_1} S_{f_2}|^2 \rangle \langle |S_{f_1+f_2}|^2 \rangle}, \quad (3)$$

where S_f is the signal evaluated at frequency f (where f can be $f_1, f_2, f_1 + f_2$) and S_f^* its complex conjugate.

Figure 5 displays the averaged bicoherence of the magnetic signal (over the last 50% of the ELM cycle), which enables the identification of the triad given by Eq. (1) (labeled in Fig. 5(b) using a red circled cross). A bicoherence of $\simeq 65\%$ clearly indicates that there is a significant nonlinear coupling between the three dominant modes. Therefore, the three-wave interaction is the likely mechanism leading to the growth of the red mode. This is consistent with a decrease of the blue mode's amplitude between the first and second half of the ELM cycle (see Fig. 2(b)). In addition, the green mode's amplitude continues to rise, during the last phase of the ELM cycle (see Fig 2(b)), which suggests that this mode's amplitude growth is dominated by the first term of Ritz model. One can then rule out contributions from the transfer component (second term in Ritz model).

Nonlinear coupling between the dominant ubiquitous pedestal modes have been studied in low frequency type

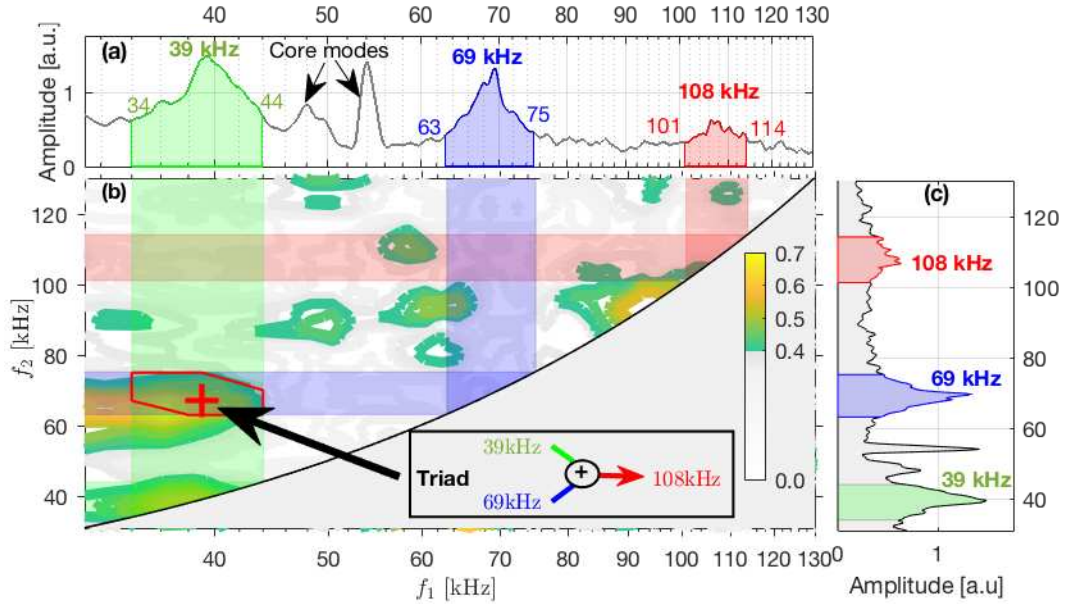


FIG. 5. Bicoherence of the magnetic signal. A log-linear plot is preferred for enhanced visualization. (a) Log-linear plot of the power spectrum. The bicoherence b^2 is plotted in (b) as a function of the two frequencies f_1 & f_2 . (c) The linear-linear plot of the power spectrum. The three dominant modes are identified in green, blue, and red and denoted with colored bands in all the plots. The time average represents the last half of the ELM cycle of Fig. 1(b). Note that the bicoherence is inherently symmetric across the $f_1 = f_2$ line (black line). We masked off the domain $f_1 \leq f_2$ for clarity. We refer the reader to Ref. [19] and references therein for a theoretical description of bicoherence.

I ELMy H-modes on the DIII-D tokamak, This letter focused on long inter-ELM phases during which the pedestal parameters are pinned to a metastable state that cannot be explained by the PB theory. Besides possibly regulating the pedestal transport [11, 26], these pedestal modes play a key role prior to the onset of ELM events. Three dominant pedestal modes, exhibiting both magnetic and density fluctuations, have been identified, and their amplitudes, frequencies, and radial profiles have been tracked during these long ELM cycle. We observed a radial shift (toward the last-closed flux surface) of the overall radial structure of the three dominant modes as the ELM event approaches. The mechanism leading to this radial shift is explained by the growth of a mode (the red mode) via three-wave interaction. This red mode is localized near the $q = 6$ surface (near the separatrix), while the other two modes are localized near $q = 5$. The three-wave interaction is confirmed using bicoherence analysis, where the triad generating the red mode from the blue and green modes is found. This nonlinear coupling between ubiquitous pedestal modes takes place once the pedestal structure is pinned to saturated profiles in a marginally stable PB state prior to the ELM onset. For instance, previous ELM model theory work [15, 27] suggested that there is a growth of erupting fingers pushing towards the metastable region (akin to the pedestal) leading to the process called detonation: ELM event. As such, a possible hypothesis could be the generation of the red mode near $q = 6$ is connected to the generation of fingers. Since ITER is envisioned to operate with a low

natural ELM frequency [28] (3 - 4 Hz), it is conceivable that the edge parameters might be ultimately clamped in which case nonlinear coupling of pedestal modes might play a key role in the onset of ELM. The implication of the three-wave nonlinear interactions of pedestal modes, as a triggering mechanism, on the recurrence of ELMs (as discussed in Refs. [29, 30]) is beyond the scope of this paper and will be the subject of future work.

This work has been supported by the U.S. DOE under the Contracts No.DE-AC02-09CH11466, DE-FG02-08ER54999, and DE-FG02-08ER54984. This material is based upon work supported by the U.S. Department of Energy, Office of Science, Office of Fusion Energy Sciences, using the DIII-D National Fusion Facility, a DOE Office of Science user facility, under Awards DEFC02-04ER54698. DIII-D data shown in this paper can be obtained in digital format by following the links at https://fusion.gat.com/global/D3D_DMP. **Disclaimer:** This report was prepared as an account of work sponsored by an agency of the United States Government. Neither the United States Government nor any agency thereof, nor any of their employees, makes any warranty, express or implied, or assumes any legal liability or responsibility for the accuracy, completeness, or usefulness of any information, apparatus, product, or process disclosed, or represents that its use would not infringe privately owned rights. Reference herein to any specific commercial product, process, or service by trade name, trademark, manufacturer, or otherwise does not necessarily constitute or imply its endorsement, recom-

mendation, or favoring by the United States Government or any agency thereof. The views and opinions of authors

expressed herein do not necessarily state or reflect those of the United States Government or any agency thereof.

-
- [1] E. Priest, *Dynamics and Structure of Quiescent Solar Prominences* (Kluwer, Dordrecht, 1989).
 - [2] H. Zohm, Plasma Phys. Control. Fusion **38**, 105 (1996).
 - [3] J. W. Connor, Plasma Physics and Controlled Fusion **40**, 531 (1998).
 - [4] W. Suttrop, Plasma Physics and Controlled Fusion **42**, A1 (2000).
 - [5] A. W. Leonard, Physics of Plasmas (1994-present) **21**, 090501 (2014).
 - [6] P. B. Snyder, H. R. Wilson, J. R. Ferron, L. L. Lao, A. W. Leonard, T. H. Osborne, A. D. Turnbull, D. Mossessian, M. Murakami, and X. Q. Xu, Phys. of Plasmas **9**, 2037 (2002).
 - [7] C. P. Perez, H. R. Koslowski, T. C. Hender, P. Smeulders, A. Loarte, P. J. Lomas, G. Saibene, R. Sartori, M. Becoulet, T. Eich, R. J. Hastie, G. T. A. Huysmans, S. Jachmich, A. Rogister, F. C. Schüller, and J. E. contributors, Plasma Physics and Controlled Fusion **46**, 61 (2004).
 - [8] A. Diallo, J. W. Hughes, M. Greenwald, B. LaBombard, E. Davis, S.-G. Baek, C. Theiler, P. Snyder, J. Canik, J. Walk, T. Golfinopoulos, J. Terry, M. Churchill, A. Hubbard, M. Porkolab, L. Delgado-Aparicio, M. L. Reinke, A. White, and A. C.-M. team, Phys. Rev. Lett. **112**, 115001 (2014).
 - [9] F. M. Laggner, E. Wolfrum, M. Cavedon, F. Mink, E. Viezzer, M. G. Dunne, P. Manz, H. Doerk, G. Birkenmeier, R. Fischer, S. Fietz, M. Maraschek, M. Willensdorfer, F. Aumayr, the EUROfusion MST1 Team, and the ASDEX Upgrade Team, Plasma Physics and Controlled Fusion **58**, 065005 (2016).
 - [10] A. Burckhart, E. Wolfrum, R. Fischer, K. Lackner, H. Zohm, and the ASDEX Upgrade Team, Nucl. Fusion **52**, 105010 (2010).
 - [11] A. Diallo, R. J. Groebner, T. L. Rhodes, D. J. Battaglia, D. R. Smith, T. H. Osborne, J. M. Canik, W. Guttenfelder, and P. B. Snyder, Physics of Plasmas (1994-present) **22**, 056111 (2015).
 - [12] A. Kirk, D. Dunai, M. Dunne, G. Huijsmans, S. Pamela, M. Becoulet, J. Harrison, J. Hillesheim, C. Roach, and S. Saarelma, Nuclear Fusion **54**, 114012 (2014).
 - [13] S. C. Cowley, H. Wilson, O. Hurricane, and B. Fong, Plasma Physics and Controlled Fusion **45**, A31 (2003).
 - [14] H. R. Wilson and S. C. Cowley, Phys. Rev. Lett. **92**, 175006 (2004).
 - [15] C. J. Ham, S. C. Cowley, G. Brochard, and H. R. Wilson, Phys. Rev. Lett. **116**, 235001 (2016).
 - [16] A. Diallo, J. Hughes, S.-G. Baek, B. LaBombard, J. Terry, I. Cziegler, A. Hubbard, E. Davis, J. Walk, L. Delgado-Aparicio, M. Reinke, C. Theiler, R. Churchill, E. Edlund, J. Canik, P. Snyder, M. Greenwald, A. White, and the Alcator C-Mod Team, Nuclear Fusion **55**, 053003 (2015).
 - [17] X. Gao, T. Zhang, X. Han, S. Zhang, D. Kong, H. Qu, Y. Wang, F. Wen, Z. Liu, and C. Huang, Nuclear Fusion **55**, 083015 (2015).
 - [18] G. McKee, R. Ashley, R. Durst, R. Fonck, M. Jakubowski, K. Tritz, K. Burrell, C. Greenfield, and J. Robinson, Review of Scientific Instruments **70**, 913 (1999), <https://doi.org/10.1063/1.1149416>.
 - [19] C. P. Ritz, E. J. Powers, and R. D. Bengtson, Physics of Fluids B: Plasma Physics **1**, 153 (1989), <https://doi.org/10.1063/1.859082>.
 - [20] B. van Milligen, T. Kalhoff, M. Pedrosa, and C. Hidalgo, Nuclear Fusion **48**, 115003 (2008).
 - [21] R. Wilcox, B. van Milligen, C. Hidalgo, D. Anderson, J. Talmadge, F. Anderson, and M. Ramisch, Nuclear Fusion **51**, 083048 (2011).
 - [22] K. Itoh, Y. Nagashima, S. Itoh, P. Diamond, A. Fujisawa, M. Yagi, and A. Fukuyama, PHYSICS OF PLASMAS **12** (2005), 10.1063/1.2062627.
 - [23] G. Tynan, R. Moyer, M. Burin, and C. Holland, Physics of Plasmas **8**, 2691 (2001).
 - [24] F. Skiff, I. Uzun, and A. Diallo, Plasma Physics and Controlled Fusion **49**, B259 (2007).
 - [25] Y. C. Kim and E. J. Powers, IEEE Transactions on Plasma Science **7**, 120 (1979).
 - [26] M. Kotschenreuther, X. Liu, D. Hatch, S. Mahajan, A. Diallo, R. Groebner, the DIII-D team, J. Hughes, the Alcator C-mod Team, C. Maggi, S. Saarelma, V. Parail, F. Koechel, and the JET Contributors, Submitted to Nuclear Fusion (2018).
 - [27] S. C. Cowley, B. Cowley, S. A. Henneberg, and H. R. Wilson, Proceedings of the Royal Society of London A: Mathematical, Physical and Engineering Sciences **471** (2015), 10.1098/rspa.2014.0913.
 - [28] A. Loarte, G. Huijsmans, S. Futatani, L. Baylor, T. Evans, D. M. Orlov, O. Schmitz, M. Becoulet, P. Cahyna, Y. Gribov, A. Kavin, A. S. Naik, D. Campbell, T. Casper, E. Daly, H. Frerichs, A. Kischner, R. Laengner, S. Lisgo, R. Pitts, G. Saibene, and A. Wingen, Nuclear Fusion **54**, 033007 (2014).
 - [29] B. Cannas, A. Fanni, A. Murari, F. Pisano, and J. Contributors, Plasma Physics and Controlled Fusion **60**, 025010 (2018).
 - [30] A. J. Webster and R. O. Dendy, Phys. Rev. Lett. **110**, 155004 (2013).